

Spectroscopic Signature of the Aggregation-Induced Emission Phenomena Caused by Restricted Nonradiative Decay: A Theoretical Proposal

Tian Zhang,^{†,||} Huili Ma,^{†,||} Yingli Niu,[‡] Wenqiang Li,[†] Dong Wang,[†] Qian Peng,^{*,‡} Zhigang Shuai,^{*,†} and WanZhen Liang[§]

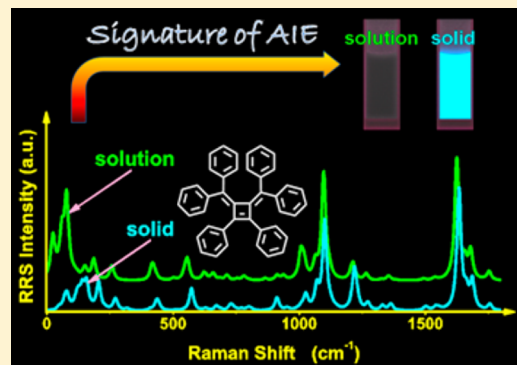
[†]Key Laboratory of Organic OptoElectronics and Molecular Engineering, Department of Chemistry, Tsinghua University, Beijing 100084, P. R. China

[‡]Key Laboratory of Organic Solids, Beijing National Laboratory for Molecular Science (BNLMS), Institute of Chemistry, Chinese Academy of Sciences, Beijing 100190, P. R. China

[§]Department of Chemistry, Xiamen University, Xiamen 361005, P. R. China

Supporting Information

ABSTRACT: It has been suggested that the exotic aggregation-induced emission (AIE) phenomenon was caused by the restriction on the nonradiative decay through intramolecular vibrational/rotational relaxation. There have been other proposed mechanisms such as J-aggregation or excimer formation, etc. Through computational studies, we propose a direct approach to verify the AIE process, namely, using resonance Raman spectroscopy (RRS) to explore the microscopic mechanism of AIE. Taking examples of AIE-active 1,2-diphenyl-3,4-bis(diphenylmethylene)-1-cyclobutene (HPDMCb) and AIE-inactive 2,3-dicyanopyrazino phenanthrene (DCPP) for comparison, we found that for the AIEgen, after aggregation into cluster, the intensities of low-frequency peaks in RRS are evidently reduced relative to the high-frequency peaks, along with a remarkable blueshift. However, the RRS of non-AIEgen remains almost unaffected upon aggregation. Such distinctive spectroscopic characteristics can be ascribed to the intramolecular vibrational relaxation which is hindered for AIEgen, especially for the low-frequency ring-twisting motions, because the RRS amplitude is proportional to the mode vibrational relaxation energy times frequency $\lambda_i \omega_i$. Thus, RRS is a direct way to clarify the recent dispute on the AIE mechanism. If such predictions are true, it will clearly validate the earlier proposed restriction on the nonradiative decay through an intramolecular vibration/rotation relaxation mechanism.



I. INTRODUCTION

Aggregation-induced emissive (AIE) or crystallization-induced emissive (CIE) luminogens are non- or low-emissive in dilute solution but highly emissive in the aggregated or crystalline state, in sharp contrast to the traditional aggregation-induced quenching (ACQ) fluorophores.^{1,2} The AIE materials have varieties of high-tech applications in the fields of light-emitting devices, chemical sensors, and biological probes.^{3–5} The AIE-active systems, i.e., AIEgens, have been found to enjoy great diversities ranging from fluorescent oligomers to pure or heteroatom-containing hydrocarbons to phosphorescent organometallic complexes.^{6,7} There have been various proposed AIE mechanisms, including restriction of intramolecular motions (RIM), conformational planarization, *E/Z* isomerization, special excimer formation, *J*-aggregate formation, twisted intramolecular charge transfer (TICT), excited-state intramolecular proton transfer (ESIPT), and conical intersection.^{8–15} Several experimental evidences have been shown to support the RIM mechanism. The earlier tests were performed through controlling the external environment such as increasing

the solvent viscosity, decreasing the solution temperature, and pressurizing the solid film.^{16,17} Then, several spectroscopy techniques such as time-resolved fluorescence spectroscopy, femtosecond pump–probe spectroscopy, and terahertz time-domain spectroscopy were introduced.^{18–20} Other computational evidence seems to be indirect and concentrated on the structural stiffening,^{21,22} although great progress has been achieved toward quantitative prediction of the radiative and nonradiative rate constants in both solution and solid phases. The restricted nonradiative intramolecular relaxation has been suggested to be the primary contributor to the AIE process.²³

Resonance Raman spectroscopy (RRS) is a spectroscopic technique in which the incident laser frequency is close to the electronic transition of the chromophore. Such frequency resonance provides a greatly enhanced Raman signal. RRS has held promise for direct characterization of the molecular

Received: February 9, 2015

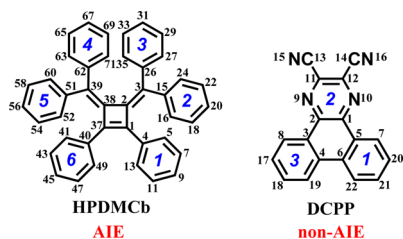
Revised: February 14, 2015

Published: February 16, 2015

excited-state dynamics, including the vibration modes and mode-specific electron–phonon couplings.²⁴ This spectroscopic technique has been used to investigate the intramolecular vibrational redistribution of the stilbene molecule, especially for the low-frequency modes.²⁵ In other words, RRS is highly sensitive to the single-molecule vibration caused by the structural changes during the excited-state relaxation process. As seen from part I in the Supporting Information (SI), under the Franck–Condon approximation and the resonance condition, the RRS intensity $\sigma(\omega)$ from the j -th normal vibrational mode is proportional to the mode's relaxation energy λ_j times the frequency ω_j : $\sigma(\omega) \propto \lambda_j \omega_j$.^{26,27} According to our previous calculations, the nonradiative decay from the excited state to the ground state is extremely fast for AIEgens because they possess a few low-frequency and high-frequency vibrational modes with large λ_j , and the formers are suppressed in aggregate. Thus, in this contribution, we stress on using RRS to detect the aggregation effect on λ_j in the nonradiative process of AIEgen, namely, to see whether λ_j 's are indeed suppressed from the solution phase to aggregate state.

1,2-Diphenyl-3,4-bis(diphenylmethylene)-1-cyclobutene (HPDMCb) is a typical AIE- and CIE-active cyclobutene derivative isolated from rubrene, and the crystalline film of HPDMCb exhibits brighter and bluer emission than its amorphous counterpart.²⁸ Deep insights into the AIE/CIE mechanism are promised to produce benefits to develop efficient solid-state blue and deep-blue emitters, which are highly pursued for high-quality full-color displays and white lightening.²⁹ Therefore, we choose HPDMCb as the model AIEgen. For contrast, we choose an AIE-inactive 2,3-dicyanopyrazino phenanthrene (DCPP)²¹ as a model non-AIEgen, for a comparative study on their RRS behaviors in solid crystal as well as in aqueous solution (Chart 1). In experiment,

Chart 1. Chemical Structure of HPDMCb and DCPP

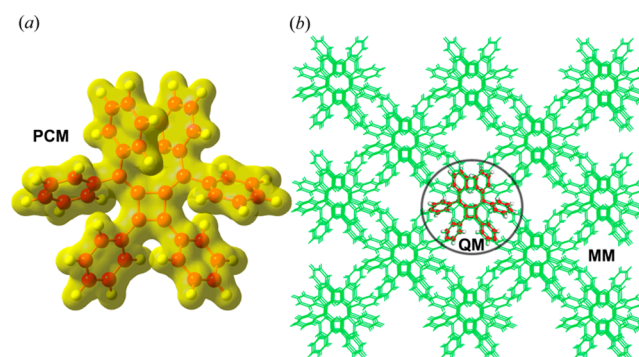


DCPP shows intensive light in pure THF solvent and weakened photoluminescence (PL) intensity in a THF–water mixture (1:9 by volume).³⁰ By pursuing the intrinsic difference of these two typical luminogens, RRS is expected to be utilized as an effective tool to examine whether the AIE mechanism is the restricted nonradiative intramolecular relaxation.

II. METHODOLOGICAL APPROACH

The computational models were built as shown in Chart 2. The bulk solvent effect has been modeled using the polarizable continuum model (PCM)³¹ implemented in the D.01 version of the Gaussian 09³² package. HPDMCb was modeled in acetonitrile solution, and DCPP was modeled in THF solution. The equilibrium solvation method was employed for geometry optimizations and vibrational frequency calculations. The nonequilibrium solvation method was used to obtain single-point vertical transition energies at the equilibrium geometry.³³ The packing surroundings in crystal are incorporated in the

Chart 2. Setup of PCM (a) and QM/MM (b) Models (Taking HPDMCb as an Example)



MM part with the general Amber force field (GAFF)³⁴ through the combined quantum mechanics and molecular mechanics (QM/MM) method. The atomic partial charges were generated by the restrained electrostatic potential (RESP)³⁵ method. The QM/MM interface was applied in the ChemShell 3.5³⁶ program, integrating Turbomole 6.5³⁷ and DL_POLY³⁸ to carry out the hybrid *ab initio*/force-field calculations. The electrostatic interaction between QM and MM is embedded in the effective Hamiltonian³⁹ and evaluated by the QM code, and the QM/MM van der Waals (vdW) interaction is calculated in the force-field expressions and managed by the MM code. During the QM/MM simulations, only the central QM molecule is active and excited, and the surrounding MM molecules are all rigid. No symmetry constraint was imposed during the optimizations in both solution and solid phases. The above PCM and QM/MM methods have been shown to be successful in dealing with varieties of AIEgens with both structure and excited-state decay rates.^{21–23} We note the recent progress toward the real-time approaches^{40,41} and excited-state *ab initio* molecular dynamics⁴² using the explicit solvation method, taking considerations of the fluctuations of the bulk solvent. The intermolecular centroid distances are shown in Figures S1 and S2 (SI). We could see these distances are close enough to exhibit nontrivial π – π stacking interactions. Then, we calculate the Coulomb coupling component of the excitonic coupling⁴³ in the MOMAP⁴⁴ program based on the electronic structure information obtained from NWChem 6.3⁴⁵ at the TD-CAM-B3LYP⁴⁶ level. The intermolecular excitonic coupling J_{coul} is found to be at least 1 order of magnitude smaller than the molecular relaxation energy $\lambda_{g(e)}$ (Tables S1 and S2, SI). Thus, in our QM/MM models, we assume the intramolecular motions dominate the photophysical process.

The equilibrium geometries and normal-mode frequencies at the local minima of S_0 and S_1 were determined by using the PBE0⁴⁷ functional together with 6-31G(d) basis set, the level of which has been benchmarked to be reliable especially for consideration of relaxation energies in the nonradiative decay process of AIEgens.²² Moreover, the PBE0 functional has been benchmarked to be one of the most accurate estimates for singlet-excited states.^{48,49} It can be seen that the low-lying S_1 states of HPDMCb and DCPP are dominated by the single excitation from HOMO to LUMO in both solution and solid phases (Figure S3, SI), the character of which is suitable for TD-DFT calculations.^{50,51} The solution-phase Hessian of S_0 was evaluated analytically at the DFT level, and that of S_1 was calculated numerically at the TD-DFT level. The solid-phase Hessians of S_0 and S_1 were obtained with the two-point

Table 1. Calculated Vertical Transition Energy (E_{vert}), Electric Transition Dipole Moment (μ_0), Oscillator Strength (f), and HOMO \rightarrow LUMO Assignments for HPDMCb and DCPD in Both Solution and Solid Phases^a

HPDMCb		E_{vert}	expt.	μ_0	f	HOMO \rightarrow LUMO
solution	absorption	3.66 eV (339 nm)	N. A.	4.96 D	0.3408	95.1%
	emission	2.38 eV (521 nm)	N. A.	6.20 D	0.3516	97.7%
solid	absorption	3.61 eV (343 nm)	3.50 eV (354 nm) ^b	5.10 D	0.3565	96.1%
	emission	2.49 eV (497 nm)	2.62 eV (474 nm) ^b	5.59 D	0.2954	97.7%
DCPD		E_{vert}	expt.	μ_0	f	HOMO \rightarrow LUMO
solution	absorption	3.26 eV (380 nm)	3.20 eV (388 nm) ^c	0.81 D	0.0080	95.6%
	emission	2.70 eV (459 nm)	2.57 eV (482 nm) ^d	1.57 D	0.0252	99.0%
solid	absorption	3.30 eV (376 nm)	N. A.	0.63 D	0.0050	95.0%
	emission	2.71 eV (457 nm)	2.46 eV (505 nm) ^e	1.00 D	0.0103	98.6%

^aThe experimental values (expt.) are given for comparison. ^bIn crystal, ref 28. ^cIn CH₂Cl₂ solution, ref 57, note that since the absorption data are not available in THF solution in ref 30 these absorption data are the only available in solution experiment just for reference. ^dIn THF solution (4 μ M), ref 30. ^eIn THF/water mixture (1:9 by volume), ref 30.

displacement approach. Gram–Schmidt orthogonalization is used to generate the transformation matrix to project out the rotational and translational spaces in both solution and solid Hessian calculations.⁵²

III. RESULTS AND DISCUSSION

Light-emitting processes are dictated by the competition between radiative decay and nonradiative decay. The radiative decay gives rise to photons through spontaneous emission. The nonradiative decay is a nonadiabatic process, which dissipates the electronic excited-state energy into vibration. The non-radiative decay rate (k_{nr}) consists of the internal conversion rate (k_{ic}) and the intersystem crossing rate (k_{isc}). We ignore k_{isc} due to the negligibly small spin–orbital coupling (SOC) for most organic molecules with $^1(\pi, \pi^*) \rightarrow ^3(\pi, \pi^*)$ transition.⁵³ The radiative decay rate (k_{r}) can be evaluated through the Einstein spontaneous emission relationship. k_{ic} can be evaluated by using the thermal correlation functional formalism in the MOMAP⁴⁴ program. The dissipation of the electronic excited-state energy into vibration could lead to the anharmonic effect in the nonradiative decay process. It has been shown that the involved vibrational quanta decrease steadily with the degrees of freedom (number of vibration modes), justifying the applicability of the harmonic model in polyatomic molecules rather than small molecules.⁵⁴ Both mode distortion and Duschinsky rotation effects are included in the related k_{ic} formula. Detailed rate formalisms are presented in the SI. We note that the transition energy gap could significantly affect both the values of k_{r} through the vertical gap and k_{ic} via the adiabatic gap. However, the line shape of the internal conversion depends mainly on the structure and vibration information. Therefore, we recompute the excitation energies based on the optimized structures at the PBE0/6-31G(d) level, in order to best match the experimental absorption and emission maxima, and the adiabatic gap is corrected at the same time. Linear-response (LR)³³ and state-specific (SS)⁵⁵ solvation methods (LR-PCM and SS-PCM) were tested with the long-range separated CAM-B3LYP⁴⁶ functional. These results are given and compared in Tables S3–S6 (SI). Finally, the combined schemes of CAM-B3LYP/SS-PCM based on the PBE0/LR-PCM optimized structures (CAM-B3LYP/SS-PCM//PBE0/LR-PCM) and CAM-B3LYP/QMMM based on the PBE0/QMMM optimized structures (CAM-B3LYP/QMMM//PBE0/QMMM) are found to reproduce satisfactorily the excitation energies for HPDMCb in solution and in solid, respectively. PBE0/LR-PCM and PBE0/QMMM

schemes were chosen to treat the transition energies of DCPD as SS-PCM sometimes generates an unphysical value for molecules with a strong charge transfer attribute,⁵⁶ and the CAM-B3LYP functional substantially overestimates the vertical gaps. These energies (see Table 1) with the chosen suitable schemes are used in the following calculations for the decay rates and the RRS. The calculated vertical transition energies agree well with the available experimental values, and most of the absolute deviations are around 0.10 eV. It is noted that the available emission values for solid-phase DCPD are measured in the amorphous phase and not the crystalline state; therefore, the deviation of 0.25 eV is relatively larger but is still within the acceptable range. k_{r} and k_{ic} are listed in Table 2. We note that k_{r}

Table 2. Calculated k_{r} and k_{ic} ($T = 300$ K) for HPDMCb and DCPD in Both Solution and Solid Phases

300 K	HPDMCb		DCPD	
	k_{r} (s ⁻¹)	k_{ic} (s ⁻¹)	k_{r} (s ⁻¹)	k_{ic} (s ⁻¹)
solution	8.64×10^7	1.31×10^{11}	7.98×10^6	1.01×10^6
solid	7.95×10^7	2.29×10^7	3.30×10^6	0.61×10^6

($\sim fE_{\text{vert}}^2$, f is the oscillator strength, and E_{vert} is the vertical transition energy) is slightly decreased (ca. 8%) upon aggregation for HPDMCb but decreased about 59% for DCPD due to the more reduced f (see Table 1) caused by the twisted conjugation plane in the crystal (Tables S7 and S8, SI). Especially, we note that at 300 K k_{ic} is decreased by about 4 orders of magnitude from the solution to solid phase for HPDMCb. The predicted fluorescence quantum yield (Φ_{F}) [$\Phi_{\text{F}} = k_{\text{r}}/(k_{\text{r}} + k_{\text{nr}}) \approx k_{\text{r}}/(k_{\text{r}} + k_{\text{ic}})$] is increased from 0.07% in solution to 78% in the solid phase. Experimentally, HPDMCb is nonluminescent in its dilute acetonitrile solution at room temperature, with Φ_{F} as low as 0.17%. When adding a 70% volume of water to the solution, its PL peak is increased about 925-fold.²⁸ The calculated results are in good agreement with experimental quantum yield measurements, whereas for DCPD k_{ic} drops only ca. 40% due to the slightly increased adiabatic energy gap in aggregate with the slightly twisted molecular plane.

For the internal conversion process, all the vibrational modes can make contributions through both the diagonal and nondiagonal elements of the R_{kl} matrix as shown in eq S2 (SI). It can be seen from Figure S4 (SI) that the significant contributions of R_{kk} are only slightly different from the solution to solid phase for both HPDMCb and DCPD. This indicates

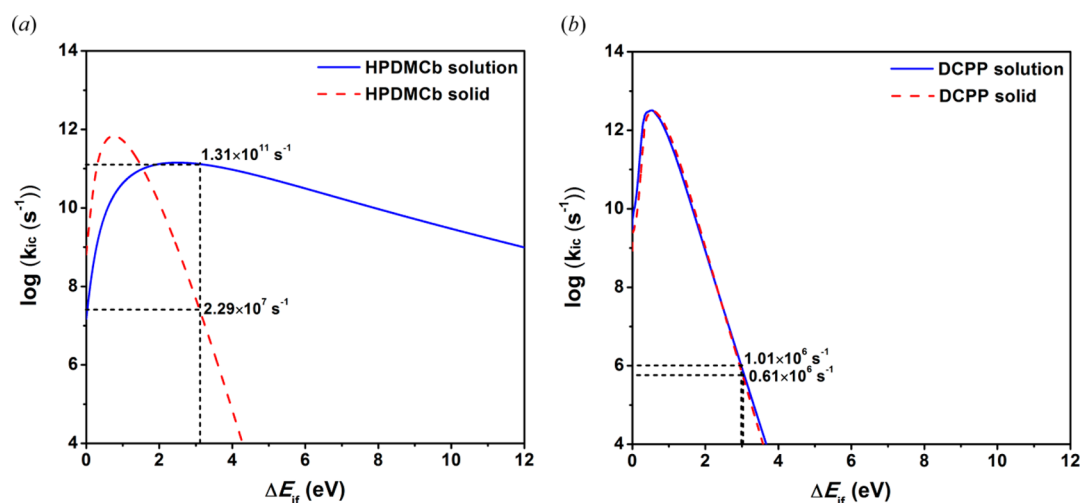


Figure 1. Internal conversion rate k_{ic} versus the energy gap ΔE_{if} in both the solution and solid phases for HPDMCb (a) and DCP (b). The vertical line indicates the position of the adiabatic energy gap E_{if} .

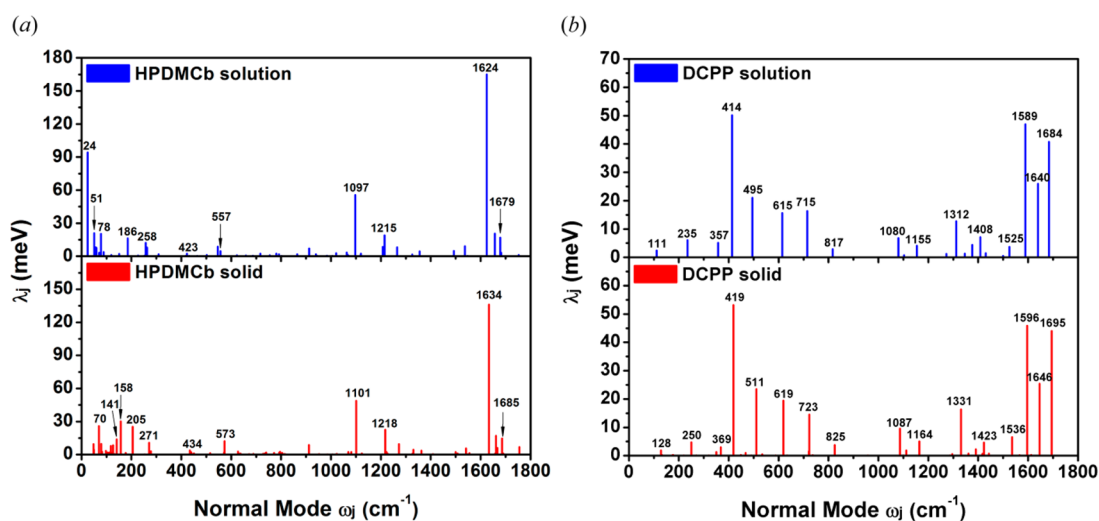


Figure 2. Calculated λ_j versus ω_j in both the solution and solid phases for HPDMCb (a) and DCP (b).

that the different k_{ic} between the solution and solid phases mainly result from the correlation function part. Assuming the existence of only one promoting vibrational mode l accepting energy of $\hbar\omega_l$, the rate can be expressed as $\log k_{ic}(\Delta E_{if}) \propto -[\Delta E_{if} - (\hbar\omega_l + \sum_{j \neq l} \lambda_j)]^2 / 2 \sum_{j \neq l} \lambda_j (2\bar{n}_j + 1)$ under the short time approximation,^{58–60} where $\bar{n}_j = 1 / [\exp(\hbar\omega_j/k_B T) - 1]$ is the phonon population. For both HPDMCb and DCP, we plot the $\log k_{ic}(\Delta E_{if})$ parabola in Figure 1. It is seen that the shape of the parabola depends on the relaxation energy $\sum_{j \neq l} \lambda_j$, and the maximum appears at $\Delta E_{if} = \hbar\omega_l + \sum_{j \neq l} \lambda_j$.²³ For HPDMCb and DCP, the adiabatic energy gap E_{if} in solution is close to those in solid. However, when going from solution to solid state, $\sum_{j \neq l} \lambda_j$ is significantly reduced for HPDMCb, resulting in much narrower parabola, leading to ca. 4 orders of magnitude decrease in k_{ic} , while for DCP, $\sum_{j \neq l} \lambda_j$ are close to each other in solution and solid phases. Thus, λ_j is an essential element to characterize both the extent of vibronic coupling and the nonradiative energy dissipation.

The total relaxation energy $\lambda_{g(e)}$ in the ground (excited) state can be expressed as a sum $\lambda_{g(e)} = \sum_{j \in g(e)} \lambda_j = \sum_{j \in g(e)} S_j \hbar\omega_j$. The Huang–Rhys factor of the j -th mode, S_j , which measures the vibrational quanta emitted or absorbed in the excited-state

relaxation process, can be calculated by the DUSHIN program.^{60,61} λ_j versus the mode frequency ω_j is depicted in Figure 2. We find that for HPDMCb frequencies of the low-frequency modes ($<100 \text{ cm}^{-1}$) become ca. 2–3-fold larger upon aggregation, e.g., 24 and 51 cm^{-1} to 70 and 141 cm^{-1} . Correspondingly, their relaxation energies are largely reduced from 94 and 21 meV to 26 and 14 meV, respectively (Table S9, SI). This indicates that the low-frequency modes tend to be suppressed by aggregation and lose the ability to dissipate the excited-state energy nonradiatively. Namely, aggregation blocks the efficient nonradiative decay channels in AIEgen dominated by the low-frequency modes. The high-frequency modes (1000–1800 cm^{-1}) are also slightly blue-shifted, e.g., 1097 vs 1101 cm^{-1} and 1624 vs 1634 cm^{-1} , and the relaxation energies show a slight decrease. The atomic movement patterns of the above-mentioned modes are shown in Figures S5 and S6 (SI). All the above behaviors upon aggregation give rise to the decrease in the total relaxation energies, leading to 4 orders of magnitude reduction in the nonradiative decay rate where $\sum_j \lambda_j$ appeared in exponent. For DCP, there are not any contributions of the low-frequency modes ($<100 \text{ cm}^{-1}$) to the total relaxation energies (Table S10, SI). Moreover, the relaxation energies in

the whole frequency region ($100\text{--}1800\text{ cm}^{-1}$) are insensitive to aggregation, which shows that aggregation changes none of the nonradiative decay channels in the non-AIEgen and can hardly affect the nonradiative rate of DCPP. The representative modes for DCPP are also illustrated in Figures S7 and S8 (SI).

The aggregation effect on the mode's relaxation dissipation of the electronic excitation energy could be further visualized through the RRS since its intensity is proportional to the mode relaxation energy λ_j multiplied by its frequency ω_j (see eq S18 in the SI). Both mode distortion and Duschinsky rotation effects are included in the related RRS formula.⁶² Detailed formalisms are shown in the SI. The Herzberg–Teller (HT) contribution^{63,64} is not considered for the molecules presented here because the transition of AIE-active HPDMCb is strong-dipole allowed; although DCPP shows a relatively weak dipole allowed transition due to its charge-transfer character with the small HOMO–LUMO overlap, the HT contribution is still quite small. This assumption is further validated via calculating the vibrationally resolved emission spectrum of DCPP including only the Franck–Condon contribution, taking example of the solution phase, by using the thermal correlation functional formalism⁶⁰ implemented in the MOMAP⁴⁴ program. It can be seen that the predicted line shape agrees well with the fluorescence experiment (Figure S9, SI). The incident wavelength for the RRS was chosen resonantly corresponding to the adiabatic transition gap. For solution-phase and solid-phase HPDMCb, 399 nm (3.11 eV) and 397 nm (3.12 eV) were adopted, respectively. For DCPP in solution and in the aggregated state, 416 nm (2.98 eV) and 412 nm (3.01 eV) were used. Damping factor γ of 100 cm^{-1} and the Lorentz broadening of 10 cm^{-1} for the delta function are applied for all RRS calculations. We then plot the calculated RRS in Figure 3 for HPDMCb and DCPP, in solution and in solid phases, respectively. Immediately, one can find that for HPDMCb the RRS lineshapes differ significantly in the low-frequency region ($<100\text{ cm}^{-1}$) between the solution phase and solid state, while the lineshapes in the high-frequency region ($1000\text{--}1800\text{ cm}^{-1}$) look similar. The low-frequency peaks show a remarkable blueshift (more than 40 cm^{-1}) after aggregation into the cluster, while the high-frequency peaks shift slightly (less than 20 cm^{-1}). For instance, peaks at 24, 51, and 78 cm^{-1} shift to 70, 141, and 158 cm^{-1} . The hypsochromic shift in the low-frequency region indicates the restricted phenyl motions in the solid phase. Meanwhile, the RRS intensities $\sigma(\omega)$ of the low-frequency peaks with respect to the high-frequency peaks decrease from the solution to solid state. From the solution to solid phase, the hypsochromic shift for the low-frequency peak with decreased relative RRS intensity indicates a reduction in λ_j since ω_j increases. The significant modes related to the Raman peaks are described and illustrated in detail in Figures S5 and S6 and Table S11 (SI). In solution, the low-frequency mode of 24 cm^{-1} with the largest relaxation energy is dominated by out-of-plane torsional movements of the phenyl 1,6,2,5-rings, while in the solid state the modes of 70 cm^{-1} are dominated by 2,5,3,4-ring twisting. Such change again indicates that twisting of phenyl 1,6-rings is restricted in the solid phase, whereas for DCPP the RRS lineshapes are quite similar in the solution state compared to the solid state, with minor shifts in position (less than 20 cm^{-1}) or intensity. The vibration characteristics for the representative modes in the solid state are the same as in the solution phase (Figures S7 and S8 and Table S12, SI). For further contrast, we make a plot of $[\sigma(\omega)/\omega]$ in Figure S10 (SI), which indeed indicates good correspondence

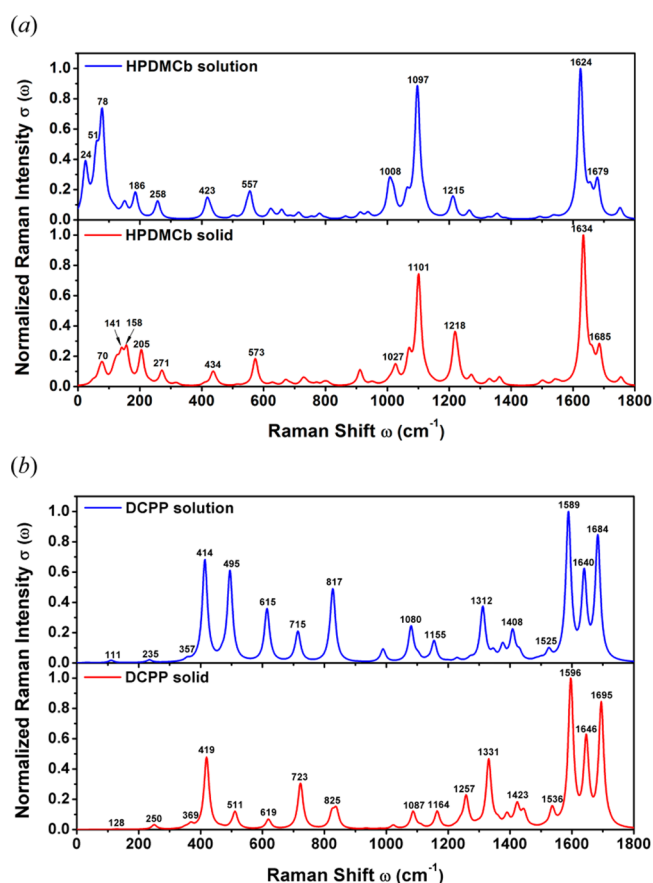


Figure 3. Calculated RRS in both solution and solid phases for HPDMCb (a) and DCPP (b).

with λ_j . It can be seen that, for HPDMCb, the proportion of the low-frequency intensity to the integrated intensity is significantly decreased by aggregation. In contrast, the low-frequency regime for DCPP is not noticeable in both solution and solid phases. Similarly, the contribution of the low-frequency vibrations ($<100\text{ cm}^{-1}$) to the total relaxation energy is largely reduced from 27% (158 meV) in solution to 10% (55 meV) in solid for HPDMCb but remains zero for DCPP (Tables S9 and S10, SI). From the molecular structural relaxation analyses, it is seen that the phenyl rings at the 1,6-positions of HPDMCb are largely hindered in the solid phase, but the “locked” ring motions of DCPP are not noticeably suppressed (Figure S11 and Tables S7 and S8, SI).

Figure 3 is depicted at the incident wavelength equal to the electronic adiabatic transition energy gap. We have also plotted RRS with other incident wavelengths, for instance, equal to the vertical transition gaps (Figures S12 and S13, SI). We find that although the line shape shows a slight modification the spectroscopic characteristics of AIEgen, namely, the blue-shifted frequency and decreased relative RRS intensity in the rigid matrix compared to solution, distinctive from non-AIEgen, are easily recognized.

IV. CONCLUSIONS

To summarize, we propose to use resonance Raman spectroscopy to test the validity of the restricted nonradiative intramolecular relaxation hypothesis in explaining the mechanism of aggregation-induced emission enhancement, through comparing the spectroscopic features for AIEgen and non-

AIEgen. This work demonstrates the potential of RRS for the characterization of the nonradiative dissipation channels in the electronic nonadiabatic transition processes and the aggregation effects. The fluorescence of molecular aggregates is a complex interplay between intramolecular (radiative and nonradiative) and intermolecular (energy transfer, charge transfer, intermolecular arrangement, and chemical contamination) pathways. This work emphasizes the intramolecular process. It shows that if the AIE phenomenon is indeed caused by the restricted nonradiative intramolecular relaxation the low-frequency peaks in RRS would hypsochromically shift (more than 40 cm^{-1}) to higher wavenumbers, along with decreased intensities relative to the high-frequency peaks in due course. The main advantage of the method presented here is the capacity to unveil the vibronic coupled electronic process beneath the resonance-enhanced Raman signals, which opens a new perspective and builds a direct bridge of understanding the photophysical characteristics. The excitonic effect as well as charge transfer delocalization processes considering the spectroscopy and nonradiative decay rates of multichromophoric aggregates are currently under investigation.

■ ASSOCIATED CONTENT

Supporting Information

Complete references 4, 13, 28, 32, 36, and 45; theoretical formalism; geometric structure; normal-mode analysis. This material is available free of charge via the Internet at <http://pubs.acs.org>.

■ AUTHOR INFORMATION

Corresponding Authors

*Q. Peng. Tel.: +86-10-82616830. E-mail: qpeng@iccas.ac.cn.

*Z. Shuai. Tel.: +86-10-62797689. E-mail: zgshuai@tsinghua.edu.cn.

Author Contributions

[†]These authors contributed equally.

Notes

The authors declare no competing financial interest.

■ ACKNOWLEDGMENTS

This work is supported by the Ministry of Science and Technology of China through 973 program (Grant Nos. 2013CB834703 and 2015CB655002) and the National Natural Science Foundation of China (Grant Nos. 21290191, 21303213, and 91333202).

■ REFERENCES

- (1) Tang, B. Z.; Zhan, X. W.; Yu, G.; Lee, P. P. S.; Liu, Y. Q.; Zhu, D. B. Efficient Blue Emission from Siloles. *J. Mater. Chem.* **2001**, *11*, 2974–2978.
- (2) Dong, Y. Q.; Lam, J. W. Y.; Qin, A. J.; Li, Z.; Sun, J. Z.; Sung, H. H. Y.; Williams, I. D.; Tang, B. Z. Switching the Light Emission of (4-Biphenyl)Phenylidibenzofulvene by Morphological Modulation: Crystallization-Induced Emission Enhancement. *Chem. Commun.* **2007**, 40–42.
- (3) Gao, F.; Liao, Q.; Xu, Z.-Z.; Yue, Y.-H.; Wang, Q.; Zhang, H.-L.; Fu, H.-B. Strong Two-Photon Excited Fluorescence and Stimulated Emission from an Organic Single Crystal of an Oligo(Phenylene Vinylene). *Angew. Chem., Int. Ed.* **2010**, *49*, 732–735.
- (4) Chen, S. J.; Hong, Y. N.; Liu, Y.; Liu, J. Z.; Leung, C. W. T.; Li, M.; Kwok, R. T. K.; Zhao, E. G.; Lam, J. W. Y.; Yu, Y.; et al. Full-Range Intracellular pH Sensing by an Aggregation-Induced Emission-Active Two-Channel Ratiometric Fluorogen. *J. Am. Chem. Soc.* **2013**, *135*, 4926–4929.

- (5) Ding, D.; Li, K.; Liu, B.; Tang, B. Z. Bioprobes Based on AIE Fluorogens. *Acc. Chem. Res.* **2013**, *46*, 2441–2453.

- (6) Oelkrug, D.; Tompert, A.; Gierschner, J.; Egelhaaf, H.-J.; Hanack, M.; Hohloch, M.; Steinhuber, E. Tuning of Fluorescence in Films and Nanoparticles of Oligophenylenevinyls. *J. Phys. Chem. B* **1998**, *102*, 1902–1907.

- (7) Hong, Y. N.; Lam, J. W. Y.; Tang, B. Z. Aggregation-Induced Emission. *Chem. Soc. Rev.* **2011**, *40*, 5361–5388.

- (8) Mei, J.; Hong, Y. N.; Lam, J. W. Y.; Qin, A. J.; Tang, Y. H.; Tang, B. Z. Aggregation-Induced Emission: The Whole Is More Brilliant than the Parts. *Adv. Mater.* **2014**, *26*, 5429–5479.

- (9) Sonoda, Y.; Tsuzuki, S.; Goto, M.; Tohnai, N.; Yoshida, M. Fluorescence Spectroscopic Properties of Nitro-Substituted Diphenylpolyenes: Effects of Intramolecular Planarization and Intermolecular Interactions in Crystals. *J. Phys. Chem. A* **2010**, *114*, 172–182.

- (10) Xie, Z. Q.; Yang, B.; Cheng, G.; Liu, L. L.; He, F.; Shen, F. Z.; Ma, Y. G.; Liu, S. Y. Supramolecular Interactions Induced Fluorescence in Crystal: Anomalous Emission of 2,5-Diphenyl-1,4-distyrylbenzene with All *cis* Double Bonds. *Chem. Mater.* **2005**, *17*, 1287–1289.

- (11) Liu, Y.; Tao, X. T.; Wang, F. Z.; Shi, J. H.; Sun, J. L.; Yu, W. T.; Ren, Y.; Zou, D. C.; Jiang, M. H. Intermolecular Hydrogen Bonds Induce Highly Emissive Excimers: Enhancement of Solid-state Luminescence. *J. Phys. Chem. C* **2007**, *111*, 6544–6549.

- (12) Choi, S.; Bouffard, J.; Kim, Y. Aggregation-Induced Emission Enhancement of a Meso-Trifluoromethyl BODIPY via J-Aggregation. *Chem. Sci.* **2014**, *5*, 751–755.

- (13) Hu, R. R.; Lager, E.; Aguilar-Aguilar, A.; Liu, J. Z.; Lam, J. W. Y.; Sung, H. H. Y.; Williams, I. D.; Zhong, Y. C.; Wong, K. S.; Peña-Cabrera, E.; et al. Twisted Intramolecular Charge Transfer and Aggregation-Induced Emission of BODIPY Derivatives. *J. Phys. Chem. C* **2009**, *113*, 15845–15853.

- (14) Kim, T. H.; Choi, M. S.; Sohn, B.-H.; Park, S.-Y.; Lyoo, W. S.; Lee, T. S. Gelation-Induced Fluorescence Enhancement of Benzoxazole-Based Organogel and its Naked-Eye Fluoride Detection. *Chem. Commun.* **2008**, 2364–2366.

- (15) Li, Q. S.; Blancafort, L. A Conical Intersection Model to Explain Aggregation Induced Emission in Diphenyl Dibenzofulvene. *Chem. Commun.* **2013**, *49*, 5966–5968.

- (16) Chen, J. W.; Law, C. C. W.; Lam, J. W. Y.; Dong, Y. P.; Lo, S. M. F.; Williams, I. D.; Zhu, D. B.; Tang, B. Z. Synthesis, Light Emission, Nanoaggregation, and Restricted Intramolecular Rotation of 1,1-Substituted 2,3,4,5-Tetraphenylsiloles. *Chem. Mater.* **2003**, *15*, 1535–1546.

- (17) Fan, X.; Sun, J. L.; Wang, F. Z.; Chu, Z. Z.; Wang, P.; Dong, Y. Q.; Hu, R. R.; Tang, B. Z.; Zou, D. C. Photoluminescence and Electroluminescence of Hexaphenylsilole are Enhanced by Pressurization in the Solid State. *Chem. Commun.* **2008**, 2989–2991.

- (18) Ren, Y.; Dong, Y. Q.; Lam, J. W. Y.; Tang, B. Z.; Wong, K. S. Studies on the Aggregation-Induced Emission of Silole Film and Crystal by Time-Resolved Fluorescence Technique. *Chem. Phys. Lett.* **2005**, *402*, 468–473.

- (19) Virgili, T.; Forni, A.; Cariati, E.; Pasini, D.; Botta, C. Direct Evidence of Torsional Motion in an Aggregation-Induced Emissive Chromophore. *J. Phys. Chem. C* **2013**, *117*, 27161–27166.

- (20) Parrott, E. P. J.; Tan, N. Y.; Hu, R. R.; Zeitler, J. A.; Tang, B. Z.; Pickwell-MacPherson, E. Direct Evidence to Support the Restriction of Intramolecular Rotation Hypothesis for the Mechanism of Aggregation-Induced Emission: Temperature Resolved Terahertz Spectra of Tetraphenylethene. *Mater. Horiz.* **2014**, *1*, 251–258.

- (21) Wu, Q. Y.; Deng, C. M.; Peng, Q.; Niu, Y. L.; Shuai, Z. G. Quantum Chemical Insights into the Aggregation Induced Emission Phenomena: A QM/MM Study for Pyrazine Derivatives. *J. Comput. Chem.* **2012**, *33*, 1862–1869.

- (22) Wu, Q. Y.; Zhang, T.; Peng, Q.; Wang, D.; Shuai, Z. G. Aggregation Induced Blue-Shifted Emission – the Molecular Picture from a QM/MM Study. *Phys. Chem. Chem. Phys.* **2014**, *16*, 5545–5552.

- (23) Shuai, Z. G.; Peng, Q. Excited States Structure and Processes: Understanding Organic Light-Emitting Diodes at the Molecular Level. *Phys. Rep.* **2014**, *537*, 123–156.
- (24) Myers, A. B. Resonance Raman Intensity Analysis of Excited-State Dynamics. *Acc. Chem. Res.* **1997**, *30*, 519–527.
- (25) Weigel, A.; Ernsting, N. P. Excited Stilbene: Intramolecular Vibrational Redistribution and Solvation Studied by Femtosecond Stimulated Raman Spectroscopy. *J. Phys. Chem. B* **2010**, *114*, 7879–7893.
- (26) Heller, E. J.; Sundberg, R.; Tannor, D. Simple Aspects of Raman Scattering. *J. Phys. Chem.* **1982**, *86*, 1822–1833.
- (27) Santoro, F.; Cappelli, C.; Barone, V. Effective Time-Independent Calculations of Vibrational Resonance Raman Spectra of Isolated and Solvated Molecules Including Duschinsky and Herzberg-Teller Effects. *J. Chem. Theory Comput.* **2011**, *7*, 1824–1839.
- (28) Dong, Y. Q.; Lam, J. W. Y.; Qin, A. J.; Sun, J. X.; Liu, J. Z.; Li, Z.; Sun, J. Z.; Sung, H. H. Y.; Williams, I. D.; Kwok, H. S.; et al. Aggregation-Induced and Crystallization-Enhanced Emissions of 1,2-Diphenyl-3,4-bis(Diphenylmethylene)-1-Cyclobutene. *Chem. Commun.* **2007**, 3255–3257.
- (29) Huang, J.; Sun, N.; Chen, P. Y.; Tang, R. L.; Li, Q. Q.; Ma, D. G.; Li, Z. Largely Blue-Shifted Emission through Minor Structural Modifications: Molecular design, Synthesis, Aggregation-Induced Emission and Deep-Blue OLED Application. *Chem. Commun.* **2014**, *50*, 2136–2138.
- (30) Qin, A. J.; Lam, J. W. Y.; Mahtab, F.; Jim, C. K. W.; Tang, L.; Sun, J. Z.; Sung, H. H. Y.; Williams, I. D.; Tang, B. Z. Pyrazine Luminogens with “Free” and “Locked” Phenyl Rings: Understanding of Restriction of Intramolecular Rotation as a Cause for Aggregation-Induced Emission. *Appl. Phys. Lett.* **2009**, *94*, 253308.
- (31) Tomasi, J.; Mennucci, B.; Cammi, R. Quantum Mechanical Continuum Solvation Models. *Chem. Rev.* **2005**, *105*, 2999–3094.
- (32) Frisch, M. J.; Trucks, G. W.; Schlegel, H. B.; Scuseria, G. E.; Robb, M. A.; Cheeseman, J. R.; Scalmani, G.; Barone, V.; Mennucci, B.; Petersson, G. A.; et al. *Gaussian 09*, Revision D.01; Gaussian, Inc.: Wallingford, CT, 2013.
- (33) Cammi, R.; Corni, S.; Mennucci, B.; Tomasi, J. Electronic Excitation Energies of Molecules in Solution: State Specific and Linear Response Methods for Nonequilibrium Continuum Solvation Models. *J. Chem. Phys.* **2005**, *122*, 104513.
- (34) Wang, J. M.; Wolf, R. M.; Caldwell, J. W.; Kollman, P. A.; Case, D. A. Development and Testing of a General Amber Force Field. *J. Comput. Chem.* **2004**, *25*, 1157–1174.
- (35) Bayly, C. I.; Cieplak, P.; Cornell, W.; Kollman, P. A. A Well-Behaved Electrostatic Potential Based Method Using Charge Restraints for Deriving Atomic Charges: the RESP Model. *J. Phys. Chem.* **1993**, *97*, 10269–10280.
- (36) Sherwood, P.; de Vries, A. H.; Guest, M. F.; Schreckenbach, G.; Catlow, C. R. A.; French, S. A.; Sokol, A. A.; Bromley, S. T.; Thiel, W.; Turner, A. J.; et al. QUASI: A General Purpose Implementation of the QM/MM Approach and Its Application to Problems in Catalysis. *J. Mol. Struct.: Theochem* **2003**, *632*, 1–28.
- (37) Ahlrichs, R.; Bär, M.; Häser, M.; Horn, H.; Kölmel, C. Electronic Structure Calculations on Workstation Computers: The Program System Turbomole. *Chem. Phys. Lett.* **1989**, *162*, 165–169.
- (38) Smith, W.; Forester, T. R. DL_POLY_2.0: A General-Purpose Parallel Molecular Dynamics Simulation Package. *J. Mol. Graph.* **1996**, *14*, 136–141.
- (39) Bakowies, D.; Thiel, W. Hybrid Models for Combined Quantum Mechanical and Molecular Mechanical Approaches. *J. Phys. Chem.* **1996**, *100*, 10580–10594.
- (40) Nguyen, P. D.; Ding, F.; Fischer, S. A.; Liang, W.; Li, X. Solvated First-Principles Excited-State Charge-Transfer Dynamics with Time-Dependent Polarizable Continuum Model and Solvent Dielectric Relaxation. *J. Phys. Chem. Lett.* **2012**, *3*, 2898–2904.
- (41) Ding, F.; Van Kuiken, B. E.; Eichinger, B. E.; Li, X. An Efficient Method for Calculating Dynamical Hyperpolarizabilities Using Real-Time Time-Dependent Density Functional Theory. *J. Chem. Phys.* **2013**, *138*, 064104.
- (42) Petrone, A.; Donati, G.; Caruso, P.; Rega, N. Understanding THz and IR Signals beneath Time-Resolved Fluorescence from Excited-State Ab Initio Dynamics. *J. Am. Chem. Soc.* **2014**, *136*, 14866–14874.
- (43) Hsu, C.-P.; You, Z.-Q.; Chen, H.-C. Characterization of the Short-Range Couplings in Excitation Energy Transfer. *J. Phys. Chem. C* **2008**, *112*, 1204–1212.
- (44) Shuai, Z. G.; Peng, Q.; Niu, Y. L.; Geng, H. MOMAP, a free and open-source molecular materials property prediction package; Revision 0.2.004; available online: <http://www.shuaigroup.net/>, Beijing, China, 2014.
- (45) Valiev, M.; Bylaska, E. J.; Govind, N.; Kowalski, K.; Straatsma, T. P.; Van Dam, H. J. J.; Wang, D.; Nieplocha, J.; Apra, E.; Windus, T. L.; et al. NWChem: A Comprehensive and Scalable Open-Source Solution for Large Scale Molecular Simulations. *Comput. Phys. Commun.* **2010**, *181*, 1477–1489.
- (46) Yanai, T.; Tew, D. P.; Handy, N. C. A New Hybrid Exchange-Correlation Functional Using the Coulomb-Attenuating Method (CAM-B3LYP). *Chem. Phys. Lett.* **2004**, *393*, 51–57.
- (47) Adamo, C.; Barone, V. Toward Reliable Density Functional Methods without Adjustable Parameters: The PBE0Model. *J. Chem. Phys.* **1999**, *110*, 6158–6170.
- (48) Jacquemin, D.; Wathélet, V.; Perpète, E. A.; Adamo, C. Extensive TD-DFT Benchmark: Singlet-Excited States of Organic Molecules. *J. Chem. Theory Comput.* **2009**, *5*, 2420–2435.
- (49) Ya. Freidzon, A.; Safonov, A. A.; Bagaturyants, A. A.; Alifimov, M. V. Solvatofluorochromism and Twisted Intramolecular Charge-Transfer State of the Nile Red Dye. *Int. J. Quantum Chem.* **2012**, *112*, 3059–3067.
- (50) Dreuw, A.; Head-Gordon, M. Single-Reference ab Initio Methods for the Calculation of Excited States of Large Molecules. *Chem. Rev.* **2005**, *105*, 4009–4037.
- (51) Adamo, C.; Jacquemin, D. The Calculations of Excited-State Properties with Time-Dependent Density Functional Theory. *Chem. Soc. Rev.* **2013**, *42*, 845–856.
- (52) Ochterski, J. W. *Vibrational Analysis in Gaussian*; Gaussian, Inc.: Wallingford, CT, 1999.
- (53) Klessinger, M.; Michl, J. *Excited States and Photochemistry of Organic Molecules*; VCH Publishers, Inc.: New York, USA, 2013.
- (54) Jiang, Y. Q.; Peng, Q.; Gao, X.; Shuai, Z. G.; Niu, Y. L.; Lin, S. H. Theoretical Design of Polythiophenevinylene Derivatives for Improvements of Light-Emitting and Photovoltaic Performances. *J. Mater. Chem.* **2012**, *22*, 4491–4501.
- (55) Improta, R.; Barone, V.; Scalmani, G.; Frisch, M. J. A State-Specific Polarizable Continuum Model Time Dependent Density Functional Theory Method for Excited State Calculations in Solution. *J. Chem. Phys.* **2006**, *125*, 054103.
- (56) Chibani, S.; Charaf-Eddin, A.; Le Guennic, B.; Jacquemin, D. Boranil and Related NBO Dyes: Insights From Theory. *J. Chem. Theory Comput.* **2013**, *9*, 3127–3135.
- (57) Nishida, J.-I.; Naraso, N.; Murai, S.; Fujiwara, E.; Tada, H.; Tomura, M.; Yamashita, Y. Preparation, Characterization, and FET Properties of Novel Dicyanopyrazinoquinoxaline Derivatives. *Org. Lett.* **2004**, *6*, 2007–2010.
- (58) Lin, S. H. Rate of Interconversion of Electronic and Vibrational Energy. *J. Chem. Phys.* **1966**, *44*, 3759–3767.
- (59) Lin, S. H.; Chang, C. H.; Liang, K. K.; Chang, R.; Shiu, Y. J.; Zhang, J. M.; Yang, T. S.; Hayashi, M.; Hsu, F. C. Ultrafast Dynamics and Spectroscopy of Bacterial Photosynthetic Reaction Centers. *Adv. Chem. Phys.* **2002**, *121*, 1–88.
- (60) Shuai, Z. G.; Wang, D.; Peng, Q.; Geng, H. Computational Evaluation of Optoelectronic Properties for Organic/Carbon Materials. *Acc. Chem. Res.* **2014**, *47*, 3301–3309.
- (61) Reimers, J. R. A Practical Method for the Use of Curvilinear Coordinates in Calculations of Normal-Mode-Projected Displacements and Duschinsky Rotation Matrices for Large Molecules. *J. Chem. Phys.* **2001**, *115*, 9103–9109.
- (62) Ma, H. L.; Liu, J.; Liang, W. Z. Time-Dependent Approach to Resonance Raman Spectra Including Duschinsky Rotation and

Herzberg-Teller Effects: Formalism and Its Realistic Applications. *J. Chem. Theory Comput.* **2012**, *8*, 4474–4482.

(63) Avila Ferrer, F. J.; Santoro, F. Comparison of Vertical and Adiabatic Harmonic Approaches for the Calculation of the Vibrational Structure of Electronic Spectra. *Phys. Chem. Chem. Phys.* **2012**, *14*, 13549–13563.

(64) Santoro, F.; Lami, A.; Improta, R.; Bloino, J.; Barone, V. Effective Method for the Computation of Optical Spectra of Large Molecules at Finite Temperature Including the Duschinsky and Herzberg-Teller Effect: The Q_x Band of Porphyrin as a Case Study. *J. Chem. Phys.* **2008**, *128*, 224311.